












Spectrum and location of ongoing extreme particle acceleration in Cassiopeia A

JOOYUN WOO ¹, KAYA MORI ¹, CHARLES J. HAILEY ¹, ELIZABETH SPIRA-SAVETT ², AYA BAMBA ^{3,4,5},
BRIAN W. GREFFENSTETTE ⁶, THOMAS B. HUMENSKY ^{7,8}, RESHMI MUKHERJEE ², SAMAR SAFI-HARB ⁹,
TEA TEMIM ¹⁰ AND NAOMI TSUJI ¹¹

¹*Columbia Astrophysics Laboratory, Columbia University, 538 West 120th Street, New York, NY 10027, USA*

²*Department of Physics and Astronomy, Barnard College, 3009 Broadway, New York, NY 10027, USA*

³*Department of Physics, Graduate School of Science, The University of Tokyo, 7-3-1 Hongo, Bunkyo-ku, Tokyo, 113-0033, Japan*

⁴*Research Center for the Early Universe, School of Science, The University of Tokyo, 7-3-1 Hongo, Bunkyo-ku, Tokyo, 113-0033, Japan*

⁵*Trans-Scale Quantum Science Institute, The University of Tokyo, 7-3-1 Hongo, Bunkyo-ku, Tokyo, 113-0033, Japan*

⁶*Space Radiation Lab, California Institute of Technology, 1200 East California Boulevard, Pasadena, CA 91125, USA*

⁷*Goddard Space Flight Center, NASA, 8800 Greenbelt Road, Greenbelt, MD 20771, USA*

⁸*Department of Physics, University of Maryland, 4150 Campus Drive, College Park, MD 20742, USA*

⁹*Department of Physics and Astronomy, University of Manitoba, 30A Sifton Road, Winnipeg, MB R3T 2N2, Canada*

¹⁰*Department of Astrophysical Sciences, Princeton University, 4 Ivy Lane, Princeton, NJ 08544, USA*

¹¹*Faculty of Science, Kanagawa University, 3-27-1 Rokkakubashi, Kanagawa-ku, Yokohama-shi, Kanagawa, 221-8686, Japan*

ABSTRACT

Young supernova remnants (SNRs) are believed to be the origin of energetic cosmic rays (CRs) below the “knee” of their spectrum at ~ 3 petaelectronvolt (PeV, 10^{15} eV). Nevertheless, the precise location, duration, and operation of CR acceleration in young SNRs are open questions. Here, we report on multi-epoch X-ray observations of Cassiopeia A (Cas A), a 350-year-old SNR, in the 15–50 keV band that probes the most energetic CR electrons. The observed X-ray flux decrease ($15 \pm 1\%$), contrary to the expected $>90\%$ decrease based on previous radio, X-ray, and gamma-ray observations, provides unambiguous evidence for CR electron acceleration operating in Cas A. A temporal model for the radio and X-ray data accounting for electron cooling and continuous injection finds that the freshly injected electron spectrum is significantly harder (exponential cutoff power law index $q = 2.15$), and its cutoff energy is much higher ($E_{cut} = 36$ TeV) than the relic electron spectrum ($q = 2.44 \pm 0.03$, $E_{cut} = 4 \pm 1$ TeV). Both electron spectra are naturally explained by the recently developed modified nonlinear diffusive shock acceleration (mNLDSA) mechanism. The CR protons producing the observed gamma rays are likely accelerated at the same location by the same mechanism as those for the injected electron. The Cas A observations and spectral modeling represent the first time radio, X-ray, gamma ray and CR spectra have been self-consistently tied to a specific acceleration mechanism -mNLDSA- in a young SNR.

Keywords: Supernova remnants(1667) — Galactic cosmic rays(567) — X-ray astronomy(1810)

1. INTRODUCTION

Supernova remnants (SNRs) have been considered excellent candidates for Galactic cosmic ray (CR) accelerators due to the large energy of supernova explosions ($E_{SN} \gtrsim 10^{51}$ erg) and formation of a strong shock (Mach number $\mathcal{M} \gg 1$). In particular, at the early stage of their evolution (< 1 kyr), their fast shock velocities ($v_{sh} \sim$ several thousand km s^{-1}) and amplified magnetic fields ($B \sim$ a few hundred μG) make SNRs ideal CR accelerators. The resultant CR spectrum bears crucial information about the shock acceleration mechanism operating in SNRs and about their acceleration environments, such as shock velocity, magnetic field, and ambient matter density. The spectrum of

the most energetic CR electrons with teraelectronvolt (TeV, 10^{12} eV) energies can be probed via the X-rays they emit by gyrating around magnetic fields (synchrotron radiation). Long-term monitoring with *Chandra* revealed that some young SNRs exhibited localized year-scale increases and decreases of soft X-ray flux in the 4-6 kiloelectronvolt (keV, 10^3 eV) band by $\sim 50\%$. This rapid and extreme variability was attributed to fast electron acceleration and synchrotron cooling in a high magnetic field, $B \geq 100 \mu\text{G}$ (Uchiyama et al. 2007; Uchiyama & Aharonian 2008a; Okuno et al. 2020). However, the energetics and spectrum of CR electrons cannot be inferred from such narrow-band observations. A further complication arises due to the contamination of their soft X-ray spectrum by significant bremsstrahlung radiation of thermal electrons ($kT \sim$ a few keV).

A direct measurement of CR electrons comes from hard X-ray observations above ~ 15 keV where the contamination by thermal electrons is minimal. The spatial distribution of the most energetic CR electrons in Cassiopeia A (Cas A), a young (~ 350 years old (Fesen et al. 2006)) nearby (3.4 kpc away (Reed et al. 1995)) SNR, was first resolved by the Nuclear Spectroscopic Telescope Array (*NuSTAR*), a space-based X-ray telescope sensitive in the 3-79 keV band, with a $14''$ (full width at half maximum) angular resolution. Cas A is a bright X-ray source whose synchrotron emission from ultra-relativistic CR electrons extends up to ~ 50 keV. The 2.4 Ms of data collected in 2012-2013 showed that X-rays above 15 keV are predominantly emitted from knots Grefenstette et al. (2015) coincident with the regions that showed fast variability in the soft X-ray observations with *Chandra* (Uchiyama & Aharonian 2008a; Patnaude & Fesen 2009a; Sato et al. 2018a). In addition, these regions are located at the reverse shock rather than the forward shock, where the strongest particle acceleration is expected (Figure 2 (a)).

NuSTAR observed Cas A again in 2023 for 188 ks. Combined with archival observations (Table 1), the multi-epoch *NuSTAR* data above 15 keV obtained over a 10-yr baseline allowed us a unique opportunity to track the most extreme particle acceleration and cooling process operating in Cas A.

2. MULTI-EPOCH X-RAY ANALYSIS

2.1. Observations and data reduction

Cas A was observed by *NuSTAR* in August 2012 - December 2013 for a net exposure of 2.2 Ms in total, and in March - April 2023 for a net exposure of 188 ks in total (Table 1). We reduced the data using NuSTAR Data Analysis Software (NuSTARDAS) version 2.1.2 and CALDB version 20240325. The NuSTARDAS pipeline produces cleaned event files with good time intervals after screening the South Atlantic Anomaly (SAA) passages and applying data quality cuts. We applied the most conservative criteria for filtering the SAA passages to ensure the most stable and accurate flux measurement.

2.2. Background estimation

Since Cas A is a bright extended ($\sim 6'$ across) source, no region in the *NuSTAR* field of view ($13' \times 13'$) is truly source-free to be used for background estimation. Instead, we modeled the background of each observation using nuskybgd, a code for simulating *NuSTAR*'s background (Wik et al. 2014). *NuSTAR*'s background is comprised of three components: (1) focused cosmic X-ray background (CXB), (2) non-focused ("stray light") CXB, and (3) internal background composed of a continuum and multiple lines. (3) is predominant above 10 keV, while (2) is strongest below 10 keV (Grefenstette et al. 2015). nuskybgd generates a model for each component and normalizes it utilizing regions outside of the source where no additional emission to the background components is expected. To account for the smearing of Cas A's emission into the regions outside of the remnant due to the finite size of the PSF ($14''$ FWHM), we added a phenomenological source model to the nuskybgd background model. After normalizing, the source model was removed, and the background model was used to simulate the background spectrum in the source region (radius $3'$ circle) with the `fakeit` command in Xspec for an exposure of 10 Ms. Background images were also generated using the normalized background-only model.

2.3. Spectral analysis

We analyzed the data in the 15-50 keV band. This choice of energy range ensures negligible contribution of thermal X-rays ($kT < 4$ keV (Hwang & Laming 2012; Bleeker et al. 2001; Maeda et al. 2009b; Favata et al. 1997b; Allen et al. 1997b)) and source emission above the background level. In addition, the uncertainty of background estimation is minimized in this energy range since the predominant background component (internal background) is well understood, and the smearing of the source counts is minimal. While combining multiple archival observations may reduce statistical uncertainty in spectral shape and flux measurement, it can introduce even greater systematic uncertainties caused

Table 1. List of observations used in this analysis

Observation ID	Date	Position angle (deg)	Exposure (ks)
40001019002	2012-08-18	84	291
40021001002	2012-08-27	76	170
40021001005	2012-10-07	33	184
40021002002	2012-11-23	338	271
40021002006	2013-03-02	249	135
40021002008	2013-03-05	249	189
40021003003	2013-05-28	151	197
40021011002	2013-10-30	7	235
40021012002	2013-11-27	335	205
40021015002	2013-12-21	312	75
40021015003	2013-12-23	312	137
Total exposure (archival data)			2,089
40801003002	2023-03-24	229	92
40801013002	2023-04-04	217	95
Total exposure (new data)			188

NOTE—The exposure has been corrected for deadtime and SAA passages. For the time variability study, only two observations (observation ID 40021002006 and 40021002008, total exposure 324 ks) were used to represent the archival data.

by instrumental (different telescope pointing) and physical (source variability) effects. We first grouped the archival observations taken at similar times (and hence similar position angles) together and performed spectral analysis within each cluster. We modeled the spectra with an absorbed power law where the hydrogen column density was fixed to $N_H = 2.14 \times 10^{22} \text{ cm}^{-2}$ (Posselt & Pavlov 2022). The abundance table from Wilms et al. (2000) was used. The model fits the data well (reduced $\chi^2 \sim 1$). The best-fit power law indices were consistent between clusters within 1σ uncertainty. We then jointly analyzed all the archival observations with a cross-normalization term. The cross-normalization terms were measured to 1% precision. With respect to the focal plane module A (FPMA) spectrum of the oldest observation (observation ID 40001019002), the power-law normalization of the spectra was found to vary within $\pm 4\%$ range except for two outliers (observation ID 40021011002 and 40021015003, -8%). Therefore, we selected two representative archival observations (observation ID 40021002006 and 40021002008, total exposure 324 ks) to compare with the new observations, given the similar position angles between these observations. The two selected archival observations are referred to as the archival observations hereafter.

The best-fit power-law photon index for the archival observations is 3.42 ± 0.02 , and the 15-50 keV flux is $(4.73 \pm 0.04) \times 10^{-11} \text{ erg s}^{-1} \text{ cm}^{-2}$. The new observations after 10 years show that the spectrum became marginally harder (power-law index 3.37 ± 0.02), and the 15-50 keV flux ($(4.02 \pm 0.04) \times 10^{-11} \text{ erg s}^{-1} \text{ cm}^{-2}$) decreased by $(15 \pm 1)\%$ (Figure 1). If the flux decreased simply by electrons' synchrotron cooling, the spectrum should have become softer due to the inverse relation between synchrotron loss and electron energy. The observed marginal hardening of the X-ray spectrum, therefore, indicates that additional physical processes are operating in addition to synchrotron cooling.

2.4. Image production

We produced a counts map, background image, and exposure map for each observation and focal plane module in the 15-50 keV range. Vignetting was corrected in the exposure maps for the mean energy (32.5 keV). Flux maps were calculated by subtracting a background image from a count map and dividing it by an exposure map. Individual flux maps were combined within each epoch to generate a flux map for 2013 and 2023. We applied the Lucy-Richardson deconvolution algorithm (Richardson 1972; Lucy 1974) to the flux maps for 50 iterations using the on-axis *NuSTAR* PSF for the 20-79 keV range (Figure 2 (a) and (b)).

3. TEMPORAL SYNCHROTRON SPECTRAL ENERGY DISTRIBUTION MODELING

For the sub-petaelectronvolt (PeV, 10^{15} eV) electrons emitting synchrotron X-rays with photon energy E_γ in a highly amplified magnetic field B (0.1-1 mG), Wright et al. (1999); Atoyan et al. (2000); Berezhko et al. (2003);

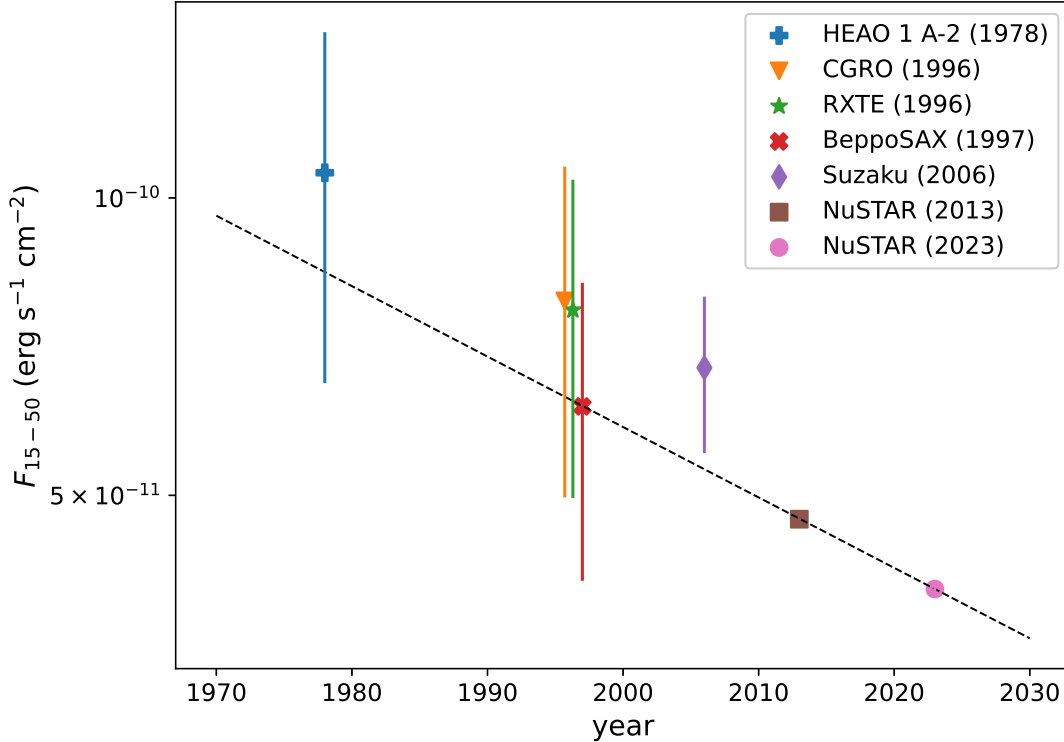


Figure 1. Historical X-ray flux of Cas A in the 15-50 keV band. The flux was calculated from the best-fit spectral model for each telescope data. The errors for the spectral model parameters were propagated to calculate the error for the flux. For HEAO 1 A-2, a power law model was fitted to the spectral data reported in Pravdo & Smith (1979). Previously reported best-fit spectral parameters were used for CGRO (The et al. 1997), RXTE (Allen et al. 1997a), BeppoSAX (Favata et al. 1997a), and Suzaku (Maeda et al. 2009a). For *NuSTAR*, the error bars are smaller than the markers. The dashed black line shows the flux decrease rate $(1.6 \pm 0.1)\% \text{ yr}^{-1}$ found from a linear regression of all the data points accounting for the error bars.

Vink & Laming (2003); Bamba et al. (2005); Uchiyama & Aharonian (2008b); Patnaude & Fesen (2009b), the synchrotron cooling time (Reynolds et al. 2018)

$$t_{1/2} = 12 \left(\frac{E_\gamma}{10 \text{ keV}} \right)^{-1/2} \left(\frac{B}{100 \mu\text{G}} \right)^{-3/2} \text{ yr} \quad (1)$$

is much shorter than the length of our baseline. Without ongoing electron acceleration, the hard X-ray flux of Cas A would have decreased by more than 90%. Instead, we observe a $(15 \pm 1)\%$ decrease in the 15-50 keV flux from the whole remnant over the past 10 years (Figure 1, uncertainties are $1-\sigma$ hereafter). The largest flux decrease is observed at the bright knots on the western rim of the reverse shock (Figure 2 (c)). Moreover, the synchrotron cooling mechanism naturally softens the radiation spectrum (producing a larger photon index Γ when $dN_\gamma/dE_\gamma \propto E_\gamma^{-\Gamma}$), whereas our spectral analysis does not find a statistically significant spectral softening in the 15-50 keV band ($\Gamma = 3.42 \pm 0.02$ in 2013 and $\Gamma = 3.37 \pm 0.02$ in 2023). Extreme electron acceleration must be operative in Cas A injecting freshly accelerated electrons. The X-ray spectrum of the injected electrons, when combined with the X-ray spectrum of the rapidly cooling preexisting electrons, leads to an essentially constant photon index with time.

To constrain the spectrum of ongoing electron acceleration in Cas A, we modeled a multiwavelength spectral energy distribution (SED) of Cas A. We first constructed the multiwavelength SED of the whole remnant using the *NuSTAR* spectrum from this work and the radio spectrum from Trotter et al. (2017) for each epoch. The radio spectrum was calculated for each epoch in the L (1395 MHz) and X (9000 MHz) band using the temporal spectral model in Trotter et al. (2017) (eq. 14, Table 5). This radio spectral model provides the best fit to the 20-yr (1995-2014) Green Bank Observatory (GBO) 40-foot L-band data and the 3-yr (2014-2017) GBO 20-m L-band and X-band data. A Gaussian quadrature sum of the $1-\sigma$ uncertainty of each model parameter was used as a $1-\sigma$ uncertainty of the radio

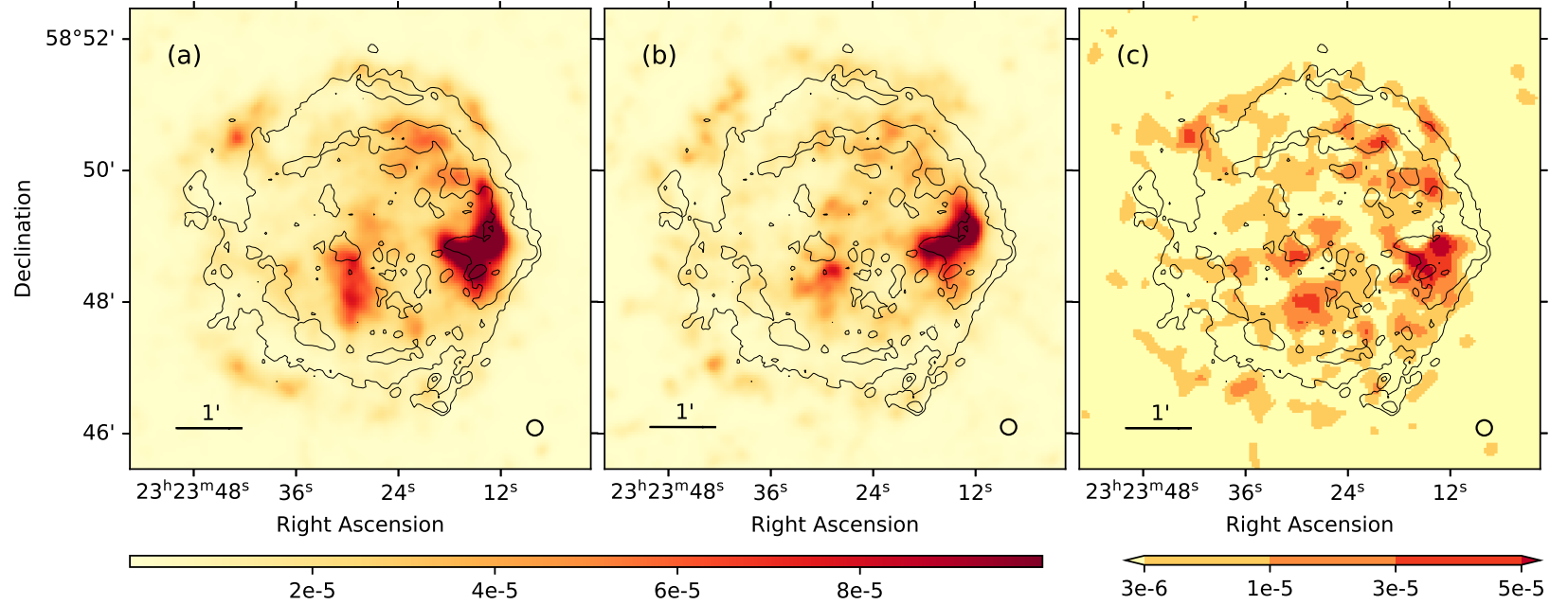


Figure 2. 15-50 keV flux maps of Cas A in 2013 (a) and 2023 (b), and a difference map between 2013 and 2023 (c). For (a) and (b), background-subtracted counts maps were divided by vignetting-corrected exposure maps, then iteratively deconvolved using the on-axis *NuSTAR* point spread function (PSF, see §2.4). The two images were scaled equally to ensure direct comparison. (c) was generated by subtracting (b) from (a). All three images were smoothed with a Gaussian kernel ($\sigma = 3.5'' = 1.5$ pixel). The L-band radio contour (Domček et al. 2021) is overlaid in black. A circle with diameter $14''$ is overlaid at the right bottom corner of each image to indicate the size of the *NuSTAR* PSF ($14''$ FWHM). Fading over the entire remnant is clearly noticeable. Most prominently, the brightest knots inside the remnant (in the middle and on the west) dimmed significantly.

spectrum (eq. 15, Table 5). The radio flux variability calculated from this model is 8% and 6% decrease in the L and X bands, respectively.

3.1. SED model description

The SED was modeled with a synchrotron radiation spectrum in a Gaussian turbulent magnetic field (Derishev & Aharonian 2019). A recent X-ray polarization measurement by the Imaging X-ray Polarimetry Explorer (IXPE) (Vink et al. 2022b) suggests magnetic turbulence in Cas A on a scale smaller than ~ 0.4 pc (IXPE angular resolution $24''$ at the source distance 3.4 kpc). A Gaussian distribution of the magnetic field strength in an SNR is theoretically motivated (e.g., Bykov et al. (2008)). The magnetic field distribution is assumed unchanged between 2013 and 2023. Nonthermal electrons present in 2013 (“preexisting electrons”) are modeled with an exponential cutoff power law distribution:

$$\frac{dN}{dE} = N_0 \left(\frac{E}{1 \text{ TeV}} \right)^{-q} \exp \left(-\frac{E}{E_{cut}} \right)^\beta. \quad (2)$$

The minimum and maximum energy bound for the electron distribution were set to $E_{min} = 100$ MeV and $E_{max} = 3$ PeV, respectively. The electrons lose energy by adiabatic and synchrotron cooling every time step.

An injected electron spectrum follows an exponential cutoff power law distribution with a distinct set of parameters from preexisting electrons. N_0 is determined by normalizing the distribution to (constant injection rate) \times (time step) between the same E_{min} and E_{max} as preexisting electrons. $\beta = 2$ is held fixed to reflect the synchrotron-loss-limited electron acceleration at the Bohm limit (Zirakashvili & Aharonian 2007). These electrons are injected and lose energy every time step by adiabatic and synchrotron cooling.

The same adiabatic and synchrotron loss formulae are used for both preexisting and injected electrons. Adiabatic energy loss is

$$\dot{E}_{ad} = \frac{\langle \dot{R}_{sh} \rangle}{\langle R_{sh} \rangle} E, \quad (3)$$

where E is an electron energy, $\langle \dot{R}_{sh} \rangle / \langle R_{sh} \rangle$ is an average expansion rate of all electrons. Pitch-angle-averaged synchrotron energy loss is (Derishev & Aharonian 2019)

$$\langle \dot{E}_{syn} \rangle = \frac{4}{3} \sigma_T \left(1 - \frac{1}{\gamma} \right) \gamma^2 \frac{B_0^2}{8\pi}, \quad (4)$$

where σ_T is the Thomson cross-section, γ is an electron Lorentz factor, and B_0 is a standard deviation of a Gaussian distribution of magnetic field strength. Synchrotron loss of radio-emitting electrons is negligible ($\ll 1\%$) over the 10-year period of our consideration for any reasonable magnetic field strength $<$ a few mG. The adiabatic loss rate $\sim 0.3\% \text{ yr}^{-1}$ is necessary to reproduce the observed radio spectral variability. This rate is comparable to the average expansion rate of Cas A’s forward shock ($0.218 \pm 0.029\% \text{ yr}^{-1}$ measured with multi-epoch *Chandra* observation (Vink et al. 2022a)). On the other hand, for X-ray-emitting electrons, synchrotron loss ($\gg 50\%$) overpowers adiabatic loss in any reasonable magnetic field strength $>$ a few tens of μG .

We first find a preexisting electron spectrum that reproduces the *NuSTAR* and radio spectrum in 2013. Then an injected electron spectrum is added every time step on top of the best-fit preexisting electron spectrum, and both electron populations are cooled every time step to reproduce the *NuSTAR* and radio spectrum in 2023. The size of the time step is $\min(0.1 \text{ yr}, E_{max} / \dot{E}_{syn})$.

3.2. SED modeling results

Setting the injection rate to zero, magnetic field $B_0 \sim 6 \mu\text{G}$ is required for the observed 15% flux decrease in the 15-50 keV band (Figure 3 top left). This magnetic field is at least an order of magnitude smaller than the previous estimations (Wright et al. 1999; Atoyan et al. 2000; Berezhko et al. 2003; Vink & Laming 2003; Bamba et al. 2005; Uchiyama & Aharonian 2008b; Patnaude & Fesen 2009b). Inverse Compton scattering (Khangulyan et al. 2014) of the cosmic microwave background and infrared (temperature ~ 100 K, energy density 2 eV cm^{-3} (Mezger et al. 1986)) photons off the electron distribution found with this magnetic field produces significantly more gamma rays than those observed by VERITAS (Abeysekera et al. 2020) and *Fermi*-LAT (Abdollahi et al. 2022; Ballet et al. 2024) (Figure 3 top right), or MAGIC (Ahnen et al. 2017).

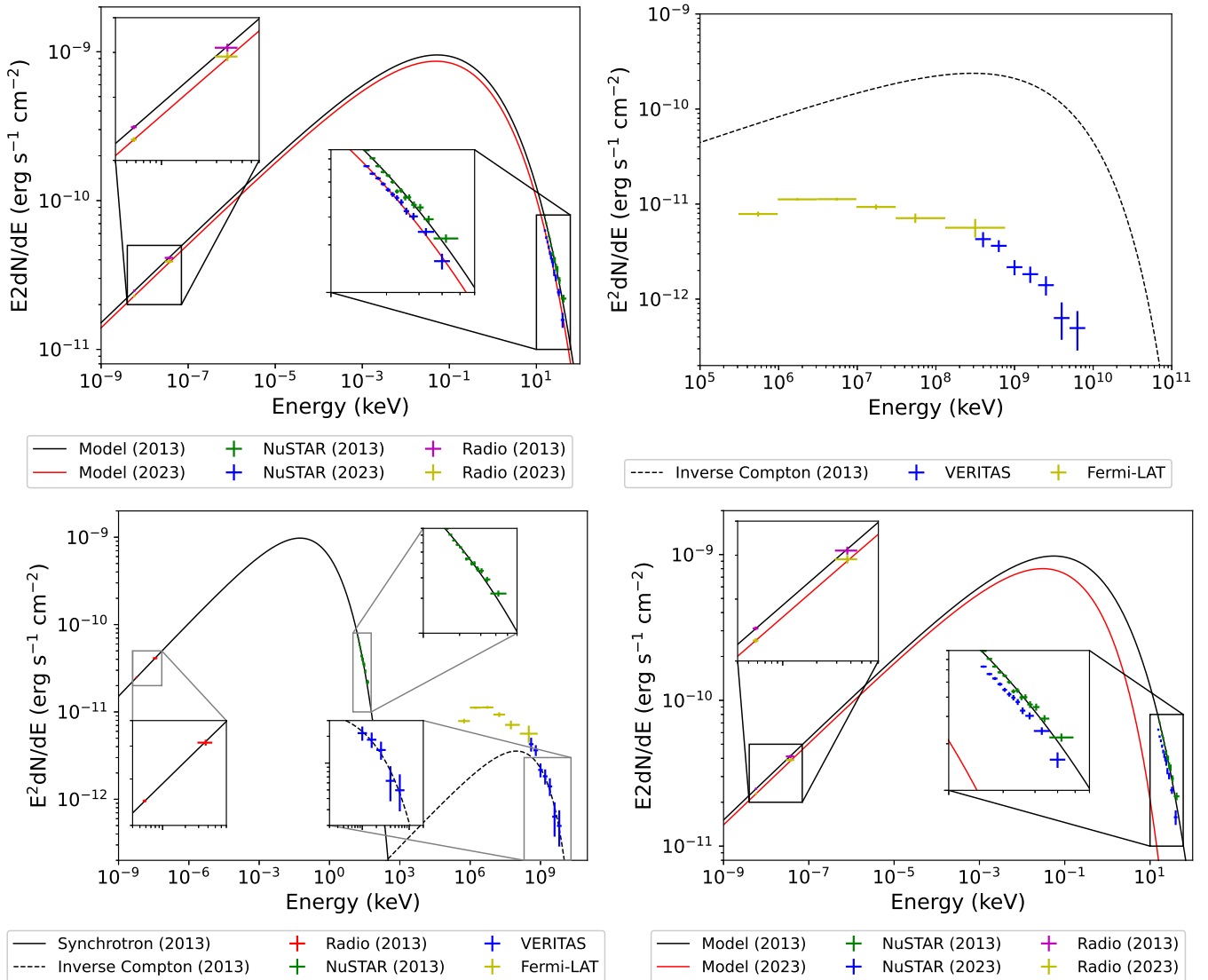


Figure 3. Top: Synchrotron (left) and inverse Compton (right) spectrum from the best-fit electron distribution for $B_0 = 6 \mu\text{G}$. With this magnetic field, the predicted gamma-ray flux significantly exceeds the observed gamma-ray flux. **Bottom: Synchrotron and inverse Compton spectrum in 2013 (left), and the synchrotron spectrum in 2013 and 2023 (right) from the best-fit electron distribution for the lower-limit magnetic field $B_0 = 123 \pm 3 \mu\text{G}$.** The lower-limit magnetic field predicts over 50% decrease in the 15-50 keV flux, much faster than the observed decrease ($15 \pm 1\%$). The *Fermi*-LAT and VERITAS spectra were taken from 4FGL-DR4 (Abdollahi et al. 2022; Ballet et al. 2024) and Abeysekara et al. (2020), respectively.

Assuming that the observed TeV gamma rays are produced entirely by inverse Compton Scattering of electrons, the lower limit on the magnetic field is found to be $B_0 = 123 \pm 8 \mu\text{G}$ (Figure 3 bottom left). This is comparable to the lower limit placed by Abeysekara et al. (2020) ($\sim 150 \mu\text{G}$) using a similar approach. The best-fit electron distribution found with this magnetic field, however, reproduces the radio and X-ray spectrum only in 2013. Due to a much faster synchrotron cooling than when $B_0 = 6 \mu\text{G}$, the predicted X-ray flux in 2023 is ~ 10 times lower, and the spectrum is much softer than the observed X-ray flux. This discrepancy between the prediction and observation leaves no possibility other than electron injection into Cas A compensating extremely rapid energy loss of preexisting electrons.

We constrain the characteristics of the preexisting and injected electron spectra using the lower-limit magnetic field found in this work ($123 \pm 8 \mu\text{G}$) and the upper-limit magnetic field established in the previous works ($B \sim 1 \text{ mG}$, Wright et al. (1999); Atoyan et al. (2000); Berezhko et al. (2003); Vink & Laming (2003); Bamba et al. (2005);

Uchiyama & Aharonian (2008b); Patnaude & Fesen (2009b)). The best-fit model parameters for preexisting and injected electrons for magnetic fields $B_0 = (123, 400, 1000) \mu\text{G}$ are listed in Table 2.

Table 2. Best-fit parameters for the synchrotron cooling and injection model

Electron population	Preexisting electrons [†]	Injected electrons		
B_0 (μG)	123 ± 8	123 ± 8	400*	1000*
q	2.44 ± 0.03	2.2	2.0	1.9
E_{cut} (TeV)	4 ± 1	36	19	12
β	0.74 ± 0.05	2*	2*	2*
Total electron energy (fraction) [‡]	$(1.09 \pm 0.02) \times 10^{49}$ erg	0.4%	0.9%	2.1%
Injection rate (10^{37} erg s ⁻¹)	—	14	4	2

NOTE—*Parameters were held fixed.

NOTE—[†]The parameters for preexisting electrons are given only for the lower-limit magnetic field $B_0 = 123 \pm 8 \mu\text{G}$. For higher magnetic fields, q and β do not change, while E_{cut} and total electron energy decrease.

NOTE—[‡]Total electron energy is reported for preexisting electrons. The fraction of the total energy of the preexisting electrons that were injected between 2012-2013 is reported for injected electrons.

4. DISCUSSION

4.1. Hard injection spectrum

For the lower-limit magnetic field of $B = 123 \mu\text{G}$, 0.4% of the total energy of the preexisting electrons needs to be injected over 10 years. The corresponding electron spectrum ($dN/dE \propto E^{-q} \exp[-E/E_{cut}]^\beta$) is significantly harder for the injected electrons ($q = 2.15$) than that of the preexisting electrons ($q = 2.44 \pm 0.03$). The cutoff energy of the spectrum is much higher for the injected electrons ($E_{cut} = 36$ TeV) than the preexisting electrons ($E_{cut} = 4 \pm 1$ TeV) (Figure 4).

For the upper-limit magnetic field of $B \sim 1$ mG, 2.1% of the preexisting electron energy needs to be injected with an even harder electron spectrum ($q = 1.86$), and cutoff energy is still higher than the preexisting electrons ($E_{cut} = 12$ TeV). The higher magnetic field produces faster synchrotron cooling, and that requires more electron injection, while the electron spectral index q and the cutoff energy E_{cut} are self-consistently regulated by the radio and *NuSTAR* data in 2023, respectively.

Further evidence that such hard-spectrum injection has been operating in Cas A comes from radio and infrared observations. Spectral hardening in the radio band has been observed since 1949 (Baars et al. 1977; Vinyaikin 2014; Trotter et al. 2017; Gorbunov et al. 2021). Spectral hardening continues in the infrared band as the infrared synchrotron flux was measured to exceed the power-law extrapolation of the radio flux (Rho et al. 2003; Jones et al. 2003). The radio-infrared spectral hardening is most significant at the bright X-ray knots where the hard-spectrum injection is expected to operate (Domček et al. 2021).

The preexisting electron spectrum reflects the entire history of electron acceleration in Cas A up to 2013. Since low-energy electrons have a cooling time scale much longer than the age of Cas A, the spectral index of the preexisting electrons is governed by the synchrotron radio spectrum of low-energy electrons. On the other hand, the injected electron spectrum reflects only the electron acceleration operating in Cas A at the current time. This is mainly determined by the fast-cooling high-energy electrons and their synchrotron hard X-ray variability.

Equivalently, the hard X-ray morphology locates only the current CR acceleration site (injected electrons), whereas the radio morphology also reveals the location of CRs accelerated in the past (preexisting electrons). The hard X-ray morphology of Cas A shows a high concentration of emission on the knots. On the other hand, the radio morphology is more isotropic with enhancement at the same knots and along the reverse shock (e.g. Domček et al. (2021)). The brightening in both wavelengths locates the knots as the current most active particle acceleration sites, while the globally isotropic radio emission traces the electrons that were accelerated at an earlier time, most likely at the forward shock, and diffused out.

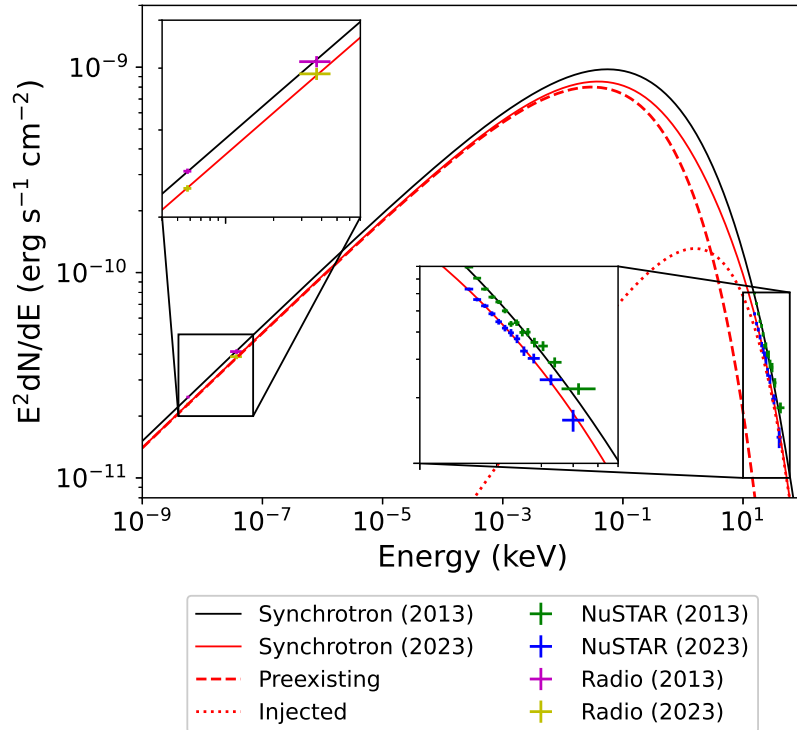


Figure 4. Synchrotron spectrum in 2013 and 2023 calculated with the temporal synchrotron cooling and injection model. The black (red) solid line is the synchrotron spectrum calculated using the best-fit parameters in Table 2 for 2013 (2023). The red dashed line is the synchrotron spectrum of the preexisting electrons in 2023, and the red dotted line shows the contribution of the injected electrons to the synchrotron spectrum in 2023. The *NuSTAR* spectrum from this work and the radio spectrum from Trotter et al. (2017) are overlaid. The error bars of the data points are for 1σ uncertainties in this figure and all the figures hereafter.

The soft-spectrum electrons that were accelerated earlier dominate the radio-emitting electron population, whereas the hard-spectrum electrons that were accelerated recently dominate the X-ray-emitting electron population. The combination of these two distinct electron populations creates a slower cutoff in the overall electron spectrum (best-fit cutoff index $\beta = 0.74 \pm 0.05$), compared with analytic solutions for synchrotron-loss-limited diffusive shock acceleration in the case of Bohm diffusion ($\beta = 2$ (Zirakashvili & Aharonian 2007)). This slow cutoff in the electron spectrum propagates to the synchrotron spectrum creating a harder X-ray spectrum than the aforementioned synchrotron-loss-limited case. There were efforts to explain this spectral behavior of Cas A by hard-spectrum ($q = 2.1$) electrons accelerated at the fast-moving jet-like structure (Zhan et al. 2022) or the jitter radiation (magnetobremsstrahlung emission of electrons in magnetic turbulence with a scale much smaller than the electron gyroradii) (Toptygin & Fleishman 1987; Medvedev 2000; Kelner et al. 2013; Greco et al. 2023). The former overpredicts the upper limits placed by LHAASO in 10 TeV - 1 PeV (Cao et al. 2024), and the latter requires a magnetic turbulence scale < 100 km, much smaller than an observable scale (e.g., IXPE angular resolution $24''$ is equivalent to $0.4 \text{ pc} = 3 \times 10^{13} \text{ km}$ at the distance 3.4 kpc). Our work provides the most natural explanation for the observed spatial-dependent spectral behavior of Cas A.

4.2. Modified nonlinear diffusive shock acceleration

One can examine if the derived CR spectra are consistent with recent theoretical expectations. Nonlinear diffusive shock acceleration (NLDSA) theories address CR-driven modification to the standard DSA by introducing a region upstream of a shock with an enhanced density due to CR pressure (“precursor”, e.g. (Drury & Voelk 1981; Drury 1983; Jones & Ellison 1991; Malkov & Drury 2001)) that leads to an increased shock compression ratio ($R > 4$). Recent hybrid (kinetic ion-fluid electron) simulations (Haggerty & Caprioli 2020; Caprioli et al. 2020) discovered that the equivalent of a precursor is formed downstream of a shock (“postcursor”) whose contribution to the increased compression ratio dominates that of a precursor. On the other hand, the compression ratio experienced by CRs is decreased since magnetic fluctuations and CRs drift away from the shock in a postcursor. This postcursor effect on the

“effective” compression ratio is parameterized by a factor α , which depends on shock velocity, upstream density, and downstream magnetic field (see Methods). Within this framework (modified NLDSA or mNLDSA), the CR spectral index is given by $q = 3R/(R - 1 - \alpha) - 2$. Typical values of $R \sim 5$ and $\alpha \sim 0.6$ (Caprioli et al. 2020) predict $q \sim 2.4$ as we found for the preexisting electron population. At the reverse shock, our inferred spectrum of $q \sim 2.2$ is consistent with the theoretical prediction if the postcursor is not present (in which case $\alpha \rightarrow 0$ and $R \rightarrow 4$). This is plausible since, at the reverse shock, the postcursor may not form due to the presence of contact discontinuity in the downstream region.

In mNLDSA, the correction factor α for shock compression ratio can be deduced from observables as (Caprioli et al. 2020)

$$\alpha \simeq 5 \frac{B}{1 \text{ mG}} \frac{1000 \text{ km s}^{-1}}{v_{sh}} \left(\frac{R \text{ cm}^{-3}}{5 n} \right)^{1/2}, \quad (5)$$

where B is a post-shock magnetic field, v_{sh} is a shock speed, R is a shock compression ratio, and n is a pre-shock plasma number density. Measuring R is nontrivial. Adopting a nominal $R = 5$ (e.g. $R \sim 4 - 7$, (Giuffrida et al. 2022)) and observed $v_{sh} \sim 6000 \text{ km s}^{-1}$ (Sato et al. 2018b; Vink et al. 2022a), $n \sim 1 \text{ cm}^{-3}$ (Lee et al. 2014), and $B = 0.7 \text{ mG}$ ($0.1 \text{ mG} \lesssim B \lesssim 1 \text{ mG}$), eq. 5 gives $\alpha \sim 0.6$.

4.3. Proton acceleration at the hard X-ray knots?

The injected electron spectrum ($q \sim 2.2$) agrees with the proton spectrum found from gamma-ray observations ($q \sim 2.2$, Abeyssekara et al. (2020)), indicating that the same acceleration mechanism is operating for both electrons and protons at the same acceleration site. The hard X-ray knots at the reverse shock are observed to move inward at a much higher speed than the forward shock ($v_{sh} \sim 8000 \text{ km s}^{-1}$ in the ejecta frame, Sato et al. (2018b); Vink et al. (2022a)) while the rest of the reverse shock is still moving outward. As it has been proposed, this requires the presence of an overdense region on the western rim of the reverse shock, such as molecular clouds (Kilpatrick et al. 2014; Frascchetti et al. 2018) or an asymmetric circumstellar shell (Orlando et al. 2022). CR protons accelerated at the reverse shock can inelastically scatter with the overdensity and produce copious gamma rays by pion production and decay.

5. SUMMARY AND CONCLUSION

Our multi-epoch hard X-ray observations enabled the isolation of a pure synchrotron radiation component of Cas A. Such radiation is associated with energetic, nonthermal CR electrons. By temporal modeling of this emission, we were able to establish the existence of two distinct populations of CR electrons. One population is more energetic and associated with a powerful, active accelerator, and the second population is less energetic and associated with an accelerator that was more active in the past. The X-ray morphology of Cas A allowed us to identify the sites of both accelerators. These observations and associated modeling provide the first self-consistent analysis of a young SNR that connects the CR spectrum and acceleration location to the broadband multiwavelength spectrum from radio to gamma-ray energies with interpretation through the most recent work on the mNLDSA theory. Our observational and theoretical approach can be applied to other young SNRs¹ to elucidate the acceleration mechanism and environment of CRs below the “knee” of their spectrum at $\sim 3 \text{ PeV}$.

¹ We thank T. Sato, D. Caprioli, R. Diesing, and S. Reynolds for the discussions. Support for this work was partially provided by NASA through *NuSTAR* Cycle 8 Guest Observer (GO) Program grant NNH21ZDA001N. J.W. was partially supported by NSF grant WOU MMA PHY-2110497.

Facilities: NuSTAR

Software: NuSTARDAS, Xspec (Arnaud 1996), NumPy (Harris et al. 2020), SciPy (Virtanen et al. 2020), Astropy (Astropy Collaboration et al. 2013, 2018, 2022), Gammapy (Donath et al. 2023; Aguasca-Cabot et al. 2023), Matplotlib (Hunter 2007), Naima (Zabalza 2015)

¹ We are conducting hard X-ray variability studies of G1.9+0.3 and Kepler using multi-epoch *NuSTAR* observation data (papers in prep). A 500-ks *NuSTAR* observation of Tycho is scheduled in 2025 (PI: J.W.), providing a 10-year baseline with the *NuSTAR* observation in 2014.

REFERENCES

- Abdollahi, S., Acero, F., Baldini, L., et al. 2022, *The Astrophysical Journal Supplement Series*, 260, 53, doi: [10.3847/1538-4365/ac6751](https://doi.org/10.3847/1538-4365/ac6751)
- Abeysekara, A. U., Archer, A., Benbow, W., et al. 2020, *The Astrophysical Journal*, 894, 51, doi: [10.3847/1538-4357/ab8310](https://doi.org/10.3847/1538-4357/ab8310)
- Aguasca-Cabot, A., Donath, A., Feijen, K., et al. 2023, *Gammapy: Python toolbox for gamma-ray astronomy*, v1.1.1, Zenodo, doi: [10.5281/zenodo.8033275](https://doi.org/10.5281/zenodo.8033275)
- Ahnen, M. L., Ansoldi, S., Antonelli, L. A., et al. 2017, *Monthly Notices of the Royal Astronomical Society*, 472, 2956, doi: [10.1093/mnras/stx2079](https://doi.org/10.1093/mnras/stx2079)
- Allen, G. E., Keohane, J. W., Gotthelf, E. V., et al. 1997a, *The Astrophysical Journal*, 487, L97, doi: [10.1086/310878](https://doi.org/10.1086/310878)
- . 1997b, *The Astrophysical Journal Letters*, 487, L97, doi: [10.1086/310878](https://doi.org/10.1086/310878)
- Arnaud, K. A. 1996, in *Astronomical Society of the Pacific Conference Series*, Vol. 101, *Astronomical Data Analysis Software and Systems V*, ed. G. H. Jacoby & J. Barnes, 17
- Astropy Collaboration, Robitaille, T. P., Tollerud, E. J., et al. 2013, *A&A*, 558, A33, doi: [10.1051/0004-6361/201322068](https://doi.org/10.1051/0004-6361/201322068)
- Astropy Collaboration, Price-Whelan, A. M., Sipőcz, B. M., et al. 2018, *AJ*, 156, 123, doi: [10.3847/1538-3881/aabc4f](https://doi.org/10.3847/1538-3881/aabc4f)
- Astropy Collaboration, Price-Whelan, A. M., Lim, P. L., et al. 2022, *ApJ*, 935, 167, doi: [10.3847/1538-4357/ac7c74](https://doi.org/10.3847/1538-4357/ac7c74)
- Atoyan, A. M., Aharonian, F. A., Tuffs, R. J., & Völk, H. J. 2000, *Astronomy and Astrophysics*, 355, 211, doi: [10.48550/arXiv.astro-ph/0001186](https://doi.org/10.48550/arXiv.astro-ph/0001186)
- Baars, J. W. M., Genzel, R., Pauliny-Toth, I. I. K., & Witzel, A. 1977, *Astronomy and Astrophysics*, 61, 99
- Ballet, J., Bruel, P., Burnett, T. H., Lott, B., & collaboration, T. F.-L. 2024, *Fermi Large Area Telescope Fourth Source Catalog Data Release 4 (4FGL-DR4)*. <https://arxiv.org/abs/2307.12546>
- Bamba, A., Yamazaki, R., Yoshida, T., Terasawa, T., & Koyama, K. 2005, *The Astrophysical Journal*, 621, 793, doi: [10.1086/427620](https://doi.org/10.1086/427620)
- Berezhko, E. G., Pühlhofer, G., & Völk, H. J. 2003, *Astronomy and Astrophysics*, 400, 971, doi: [10.1051/0004-6361:20030033](https://doi.org/10.1051/0004-6361:20030033)
- Bleeker, J. A. M., Willingale, R., van der Heyden, K., et al. 2001, *Astronomy and Astrophysics*, 365, L225, doi: [10.1051/0004-6361:20000048](https://doi.org/10.1051/0004-6361:20000048)
- Bykov, A. M., Uvarov, Y. A., & Ellison, D. C. 2008, *The Astrophysical Journal Letters*, 689, L133, doi: [10.1086/595868](https://doi.org/10.1086/595868)
- Cao, Z., Aharonian, F., An, Q., et al. 2024, *The Astrophysical Journal Letters*, 961, L43, doi: [10.3847/2041-8213/ad1d62](https://doi.org/10.3847/2041-8213/ad1d62)
- Caprioli, D., Haggerty, C. C., & Blasi, P. 2020, *The Astrophysical Journal*, 905, 2, doi: [10.3847/1538-4357/abbe05](https://doi.org/10.3847/1538-4357/abbe05)
- Derishev, E., & Aharonian, F. 2019, *The Astrophysical Journal*, 887, 181, doi: [10.3847/1538-4357/ab536a](https://doi.org/10.3847/1538-4357/ab536a)
- Domček, V., Vink, J., Hernández Santisteban, J. V., DeLaney, T., & Zhou, P. 2021, *Monthly Notices of the Royal Astronomical Society*, 502, 1026, doi: [10.1093/mnras/staa3896](https://doi.org/10.1093/mnras/staa3896)
- Donath, A., Terrier, R., Remy, Q., et al. 2023, *Astronomy and Astrophysics*, 678, A157, doi: [10.1051/0004-6361/202346488](https://doi.org/10.1051/0004-6361/202346488)
- Drury, L. O. 1983, *Reports on Progress in Physics*, 46, 973, doi: [10.1088/0034-4885/46/8/002](https://doi.org/10.1088/0034-4885/46/8/002)
- Drury, L. O., & Voelk, J. H. 1981, *The Astrophysical Journal*, 248, 344, doi: [10.1086/159159](https://doi.org/10.1086/159159)
- Favata, F., Vink, J., dal Fiume, D., et al. 1997a, *Astronomy and Astrophysics*, 324, L49, doi: [10.48550/arXiv.astro-ph/9707052](https://doi.org/10.48550/arXiv.astro-ph/9707052)
- . 1997b, *Astronomy and Astrophysics*, 324, L49, doi: [10.48550/arXiv.astro-ph/9707052](https://doi.org/10.48550/arXiv.astro-ph/9707052)
- Fesen, R. A., Hammell, M. C., Morse, J., et al. 2006, *The Astrophysical Journal*, 645, 283, doi: [10.1086/504254](https://doi.org/10.1086/504254)
- Fraschetti, F., Katsuda, S., Sato, T., Jokipii, J. R., & Giacalone, J. 2018, *Physical Review Letters*, 120, 251101, doi: [10.1103/PhysRevLett.120.251101](https://doi.org/10.1103/PhysRevLett.120.251101)
- Giuffrida, R., Miceli, M., Caprioli, D., et al. 2022, *Nature Communications*, 13, 5098, doi: [10.1038/s41467-022-32781-4](https://doi.org/10.1038/s41467-022-32781-4)
- Gorbynov, A., Sukharev, A., Ryabov, M., Bezrukovs, V., & Orbidans, A. 2021, *Galaxies*, 9, 30, doi: [10.3390/galaxies9020030](https://doi.org/10.3390/galaxies9020030)
- Greco, E., Vink, J., Ellien, A., & Ferrigno, C. 2023, *The Astrophysical Journal*, 956, 116, doi: [10.3847/1538-4357/acf567](https://doi.org/10.3847/1538-4357/acf567)
- Grefenstette, B. W., Reynolds, S. P., Harrison, F. A., et al. 2015, *The Astrophysical Journal*, 802, 15, doi: [10.1088/0004-637X/802/1/15](https://doi.org/10.1088/0004-637X/802/1/15)
- Haggerty, C. C., & Caprioli, D. 2020, *The Astrophysical Journal*, 905, 1, doi: [10.3847/1538-4357/abbe06](https://doi.org/10.3847/1538-4357/abbe06)
- Harris, C. R., Millman, K. J., van der Walt, S. J., et al. 2020, *Nature*, 585, 357, doi: [10.1038/s41586-020-2649-2](https://doi.org/10.1038/s41586-020-2649-2)
- Hunter, J. D. 2007, *Computing in Science & Engineering*, 9, 90, doi: [10.1109/MCSE.2007.55](https://doi.org/10.1109/MCSE.2007.55)
- Hwang, U., & Laming, J. M. 2012, *The Astrophysical Journal*, 746, 130, doi: [10.1088/0004-637X/746/2/130](https://doi.org/10.1088/0004-637X/746/2/130)

- Jones, F. C., & Ellison, D. C. 1991, *Space Science Reviews*, 58, 259, doi: [10.1007/BF01206003](https://doi.org/10.1007/BF01206003)
- Jones, T. J., Rudnick, L., DeLaney, T., & Bowden, J. 2003, *The Astrophysical Journal*, 587, 227, doi: [10.1086/368149](https://doi.org/10.1086/368149)
- Kelner, S. R., Aharonian, F. A., & Khangulyan, D. 2013, *The Astrophysical Journal*, 774, 61, doi: [10.1088/0004-637X/774/1/61](https://doi.org/10.1088/0004-637X/774/1/61)
- Khangulyan, D., Aharonian, F. A., & Kelner, S. R. 2014, *The Astrophysical Journal*, 783, 100, doi: [10.1088/0004-637X/783/2/100](https://doi.org/10.1088/0004-637X/783/2/100)
- Kilpatrick, C. D., Biegging, J. H., & Rieke, G. H. 2014, *The Astrophysical Journal*, 796, 144, doi: [10.1088/0004-637X/796/2/144](https://doi.org/10.1088/0004-637X/796/2/144)
- Lee, J.-J., Park, S., Hughes, J. P., & Slane, P. O. 2014, *The Astrophysical Journal*, 789, 7, doi: [10.1088/0004-637X/789/1/7](https://doi.org/10.1088/0004-637X/789/1/7)
- Lucy, L. B. 1974, *Astronomical Journal*, 79, 745, doi: [10.1086/111605](https://doi.org/10.1086/111605)
- Maeda, Y., Uchiyama, Y., Bamba, A., et al. 2009a, *Publications of the Astronomical Society of Japan*, 61, 1217, doi: [10.1093/pasj/61.6.1217](https://doi.org/10.1093/pasj/61.6.1217)
- . 2009b, *Publications of the Astronomical Society of Japan*, 61, 1217, doi: [10.1093/pasj/61.6.1217](https://doi.org/10.1093/pasj/61.6.1217)
- Malkov, M. A., & Drury, L. O. 2001, *Reports on Progress in Physics*, 64, 429, doi: [10.1088/0034-4885/64/4/201](https://doi.org/10.1088/0034-4885/64/4/201)
- Medvedev, M. V. 2000, *The Astrophysical Journal*, 540, 704, doi: [10.1086/309374](https://doi.org/10.1086/309374)
- Mezger, P. G., Tuffs, R. J., Chini, R., Kreysa, E., & Gemuend, H. P. 1986, *Astronomy and Astrophysics*, 167, 145
- Okuno, T., Tanaka, T., Uchida, H., et al. 2020, *The Astrophysical Journal*, 894, 50, doi: [10.3847/1538-4357/ab837e](https://doi.org/10.3847/1538-4357/ab837e)
- Orlando, S., Wongwathanarat, A., Janka, H. T., et al. 2022, *Astronomy and Astrophysics*, 666, A2, doi: [10.1051/0004-6361/202243258](https://doi.org/10.1051/0004-6361/202243258)
- Patnaude, D. J., & Fesen, R. A. 2009a, *The Astrophysical Journal*, 697, 535, doi: [10.1088/0004-637X/697/1/535](https://doi.org/10.1088/0004-637X/697/1/535)
- . 2009b, *The Astrophysical Journal*, 697, 535, doi: [10.1088/0004-637X/697/1/535](https://doi.org/10.1088/0004-637X/697/1/535)
- Posselt, B., & Pavlov, G. G. 2022, *The Astrophysical Journal*, 932, 83, doi: [10.3847/1538-4357/ac6dca](https://doi.org/10.3847/1538-4357/ac6dca)
- Pravdo, S. H., & Smith, B. W. 1979, *The Astrophysical Journal*, 234, L195, doi: [10.1086/183138](https://doi.org/10.1086/183138)
- Reed, J. E., Hester, J. J., Fabian, A. C., & Winkler, P. F. 1995, *The Astrophysical Journal*, 440, 706, doi: [10.1086/175308](https://doi.org/10.1086/175308)
- Reynolds, S. P., Borkowski, K. J., & Gwynne, P. H. 2018, *The Astrophysical Journal*, 856, 133, doi: [10.3847/1538-4357/aab3d3](https://doi.org/10.3847/1538-4357/aab3d3)
- Rho, J., Reynolds, S. P., Reach, W. T., et al. 2003, *The Astrophysical Journal*, 592, 299, doi: [10.1086/375564](https://doi.org/10.1086/375564)
- Richardson, W. H. 1972, *Journal of the Optical Society of America* (1917-1983), 62, 55
- Sato, T., Katsuda, S., Morii, M., et al. 2018a, *The Astrophysical Journal*, 853, 46, doi: [10.3847/1538-4357/aaa021](https://doi.org/10.3847/1538-4357/aaa021)
- . 2018b, *The Astrophysical Journal*, 853, 46, doi: [10.3847/1538-4357/aaa021](https://doi.org/10.3847/1538-4357/aaa021)
- The, L.-S., Leising, M. D., Hartmann, D. H., et al. 1997, in *AIP Conference Proceedings (AIP)*, doi: [10.1063/1.53930](https://doi.org/10.1063/1.53930)
- Toptygin, I. N., & Fleishman, G. D. 1987, *Astrophysics and Space Science*, 132, 213, doi: [10.1007/BF00641755](https://doi.org/10.1007/BF00641755)
- Trotter, A. S., Reichart, D. E., Egger, R. E., et al. 2017, *Monthly Notices of the Royal Astronomical Society*, 469, 1299, doi: [10.1093/mnras/stx810](https://doi.org/10.1093/mnras/stx810)
- Uchiyama, Y., & Aharonian, F. A. 2008a, *The Astrophysical Journal Letters*, 677, L105, doi: [10.1086/588190](https://doi.org/10.1086/588190)
- . 2008b, *The Astrophysical Journal Letters*, 677, L105, doi: [10.1086/588190](https://doi.org/10.1086/588190)
- Uchiyama, Y., Aharonian, F. A., Tanaka, T., Takahashi, T., & Maeda, Y. 2007, *Nature*, 449, 576, doi: [10.1038/nature06210](https://doi.org/10.1038/nature06210)
- Vink, J., & Laming, J. M. 2003, *The Astrophysical Journal*, 584, 758, doi: [10.1086/345832](https://doi.org/10.1086/345832)
- Vink, J., Patnaude, D. J., & Castro, D. 2022a, *The Astrophysical Journal*, 929, 57, doi: [10.3847/1538-4357/ac590f](https://doi.org/10.3847/1538-4357/ac590f)
- Vink, J., Prokhorov, D., Ferrazzoli, R., et al. 2022b, *The Astrophysical Journal*, 938, 40, doi: [10.3847/1538-4357/ac8b7b](https://doi.org/10.3847/1538-4357/ac8b7b)
- Vinyaikin, E. N. 2014, *Astronomy Reports*, 58, 626, doi: [10.1134/S1063772914090078](https://doi.org/10.1134/S1063772914090078)
- Virtanen, P., Gommers, R., Oliphant, T. E., et al. 2020, *Nature Methods*, 17, 261, doi: [10.1038/s41592-019-0686-2](https://doi.org/10.1038/s41592-019-0686-2)
- Wik, D. R., Hornstrup, A., Molendi, S., et al. 2014, *The Astrophysical Journal*, 792, 48, doi: [10.1088/0004-637X/792/1/48](https://doi.org/10.1088/0004-637X/792/1/48)
- Wilms, J., Allen, A., & McCray, R. 2000, *The Astrophysical Journal*, 542, 914, doi: [10.1086/317016](https://doi.org/10.1086/317016)
- Wright, M., Dickel, J., Koralesky, B., & Rudnick, L. 1999, *The Astrophysical Journal*, 518, 284, doi: [10.1086/307270](https://doi.org/10.1086/307270)
- Zabalza, V. 2015, *Proc. of International Cosmic Ray Conference 2015*, 922
- Zhan, S., Wang, W., Mou, G., & Li, Z. 2022, *Monthly Notices of the Royal Astronomical Society*, 513, 2471, doi: [10.1093/mnras/stac970](https://doi.org/10.1093/mnras/stac970)
- Zirakashvili, V. N., & Aharonian, F. 2007, *Astronomy and Astrophysics*, 465, 695, doi: [10.1051/0004-6361:20066494](https://doi.org/10.1051/0004-6361:20066494)